First-principles simulations of the fluorescence modulation of a COX-2 specific fluorogenic probe upon protein dimerization for cancer discrimination

Álex Pérez-Sánchez[1], Carles Curutchet[2,3,*], Àngels González-Lafont[1,4,*] and José M. Lluch[1,4]

[1]Departament de Química, Universitat Autònoma de Barcelona, 08193 Bellaterra, Barcelona, Spain
[2]Departament de Farmàcia i Tecnologia Farmacèutica, i Fisicoquímica, Facultat de Farmàcia i Ciències de l'Alimentació, Universitat de Barcelona (UB), 08028 Barcelona, Spain.
[3]Institut de Química Teòrica i Computacional (IQTCUB), Universitat de Barcelona (UB), 08028 Barcelona, Spain
[4]Institut de Biotecnologia i de Biomedicina (IBB), Universitat Autònoma de Barcelona, 08193 Bellaterra, Barcelona, Spain

Emails:
Alex.Perez@uab.cat
Carles.Curutchet@ub.edu
Angels.Gonzalez@uab.cat
JoseMaria.Lluch@uab.cat

Corresponding Authors:

Àngels González-Lafont
Departament de Química, Universitat Autònoma de Barcelona, 08193 Bellaterra, Barcelona, Spain
Telephone +34 93 581 1672
Angels.Gonzalez@uab.cat

Carles Curutchet
Departament de Farmàcia i Tecnologia Farmacèutica, i Fisicoquímica, Facultat de Farmàcia i Ciències de l'Alimentació, Universitat de Barcelona (UB), 08028 Barcelona, Spain.
Telephone +34 93 402 4557
Carles.Curutchet@ub.edu

22 manuscript pages, 19 supporting information pages, 6 Figures (+23 in the SI), 1 scheme and 0 tables (+2 in the SI)

Running title: Fluorescence and COX-2 Dimerization in Cancer Detection

Supplementary Material:
- 2024_SI_PerezSanchez_Curutchet_GonzalezLafont_Lluch.docx
- QMMMpol_spectra_data.zip

Abstract

Cyclooxygenase-2 (COX-2) plays a crucial role in inflammation and has been implicated in cancer development. Understanding the behaviour of COX-2 in different cellular contexts is essential for developing targeted therapeutic strategies. In this study, we investigate the fluorescence spectrum of a fluorogenic probe, NANQ-IMC6, when bound to the active site of human COX-2 in both its monomeric and homodimeric forms. We employ a multiscale first-principles simulation protocol that combines ground state MM-MD simulations with multiple excited state adiabatic QM/MM Born-Oppenheimer MD simulations based on linear response TD-DFT, which allows to account for protein heterogeneity effects on excited-state properties. Emission is then estimated from polarizable embedding TD-DFT QM/MMPol calculations. Our findings indicate that the emission shift arises from dimerization of the highly overexpressed COX-2 in cancer tissues, in contrast to the monomer structure present in inflammatory lesions and in normal cells with constitutive COX-2. This spectral shift is linked to changes in specific protein-probe interactions upon dimerization due to changes in the environment, whereas steric effects related to modulation of the NANQ geometry by the protein scaffold are found to be minor. This research paves the way for detailed investigations on the impact of environment structural transitions on the spectral properties of fluorogenic probes. Moreover, the fact that COX-2 exists as homodimer just in cancer tissues, but as monomer elsewhere, gives novel hints for therapeutical avenues to fight cancer and contributes to the development of drugs targeted to COX-2 dimer in cancer, but without affecting constitutive COX-2, thus minimizing off-target effects.

Keywords

COX-2 dimerization, fluorogenic probes, cancer detection, inflammatory lesions, fluorescence, adiabatic excited-state simulations, molecular dynamic simulations

Broader Audience Statement

This study explores how a specific fluorescent probe interacts with COX-2, an enzyme linked to inflammation and cancer. By using first principles simulations, we rationalize the link between COX-2 dimerization and fluorescence modulation in cancer cells. This finding paves the way for the rational design of specific fluorogenic probes able to shed light on the formation of protein multimers and provides new hints on the development of improved cancer detection strategies and the design of targeted treatments with fewer side effects.

Abbreviations and symbols

AA: Arachidonic Acid (5Z,8Z,11Z,14Z-eicosatetraenoic acid)
COX-1: Cyclooxygenase 1
hCOX-2: human Cyclooxygenase 2
5-LOX: 5 Lipoxygenase
LTB4: Leukotriene B4
NSAIDs: Non-steroidal Anti-Inflammatory Drugs.
NANQ: Nitroacenaphathenequinone
IMC: Indomethacin
MM-MD: Molecular Mechanics - Molecular Dynamics
QM/MM: Quantum Mechanics/Molecular Mechanics
BOMD: Born-Oppenheimer Molecular Dynamics
TD-DFT: Time-dependent Density Functional Theory
RMSD: Root-Mean-Square Deviation
RMSF: Root-Mean-Square Fluctuation
HOMO: Highest Occupied Molecular Orbital
LUMO: Lowest Occupied Molecular Orbital
QM: Quantum Mechanics
CIS: Single Excitation Configuration Interaction
IEFPCM: Integral Equation Formalism Polarizable Continuum Model
PDB: Protein Data Bank
OPC: four-point Optimal Point Charge

1. Introduction

Inflammation constitutes a first line of defense against invading pathogens and injury. However, if inflammation occurs at the wrong times or becomes chronic, it may enhance tissue destruction, thus contributing to the development, growth and metastasis of cancers, and the inflammatory environment of tumor cells can exclude tumor-fighting immune cells. In this sense inflammation is considered a hallmark of cancer. (Fishbein et al., 2021) In the initial phase of inflammation (acute inflammation) the pro-inflammatory lipid mediators prostaglandins and leukotrienes, that derive from the arachidonic acid (AA, 5Z,8Z,11Z,14Z-eicosatetraenoic acid), are released by the action of the key pro-inflammatory enzymes, cyclooxygenase-2 (COX-2) and 5-lipoxygenase (5-LOX), respectively. The potent chemotactic agent leukotriene B4 (LTB4) promotes the polymorphonuclear neutrophil recruitment to the inflamed tissue, while the formation of prostaglandins further accelerates the inflammatory process. (Serhan & Petasis, 2011)

The current anti-inflammatory pharmacological therapies against acute inflammation are mainly based on non-steroidal anti-inflammatory drugs (NSAIDs) that inhibit COX-2. Unfortunately, they have several damaging side effects and are immunosuppressive. (Serhan & Sulciner, 2023) This a pity because a number of NSAIDs, like inhibitors of COX-2, have been proven to have potent antitumor capabilities. (Menter et al., 2010; Wen et al., 2020) However, prolonged use of non-selective COX-2 NSAIDs is associated with gastro-toxicity and renal damage, as they inhibit both constitutive COX-1 and inducible COX-2 (upregulated in inflammations). On the other hand, selective COX-2 inhibitors without gastric side-effects cause an increased risk of cardiovascular disease, especially after long-term use, because they also inhibit constitutive COX-2 (barely expressed in normal cells). Thus, this unwanted side effects have prevented the development of new drugs that target COX-2 to treat inflammation and cancer, therefore wasting the huge potential that blocking COX-2 represents for cancer prevention. (Kirkby et al., 2018) The problem is much worse in premalignant and malignant tumors, where COX-2 is expressed at significantly higher levels compared to non-cancerous inflammatory lesions (COX-2 is overexpressed a hundred times more in cancer tissues than in normal inflammations). (Zhang et al., 2013) Tumor survival and function are regulated or promoted by the tumor microenvironment (TME). TME is closely associated with inflammatory response and the inflammatory mediators in TME. Prostaglandin E2, produced by COX-2, is one of the most important inflammatory factors in TME, which is related to survival, growth, migration, invasion, angiogenesis and immune evasion of cancer cells, leading to poor response of immunotherapy. (Wang et al. 2023) Thus, a long-term effective cancer treatment based on current NSAIDs would be expected to require larger doses than those used for non-cancerous inflammations, magnifying the expected harmful side effects and absolutely precluding their use.

In this context, an attractive question is whether we can take advantage of the huge upregulation of COX-2 in cancer tissues to design specific inhibitors that do not affect the COX-2 that barely exists as constitutive in a few tissues. The answer derives from the fact that COX-2 is recognized to be a very useful cancer cell marker, and a variety of fluorescence imaging agents that efficiently target COX-2 have been developed. After injection, these agents become highly enriched in inflamed or tumor tissues, in comparison to normal tissue. This accumulation provides enough signal for *in vitro* and

in vivo fluorescence imaging. COX-2 imaging is usually realized by using a NSAID (for instance, ibuprofen, indomethacin, or celecoxib) and a fluorophore that are coupled by a suitable linker unit. The NSAID enters the corresponding binding site of COX-2. After excitation the fluorophore can re-emit fluorescent light so indicating the presence of COX-2 in inflammations and cancer tissues. (Xia et al., 2021; Kim et al., 2018; Wang et al., 2020; Luo et al., 2022) Specially interesting is the case (Zhang et al., 2013) of a COX-2-specific fluorogenic probe (NANQ-IMC6), that consists of a chemically modified indomethacin (IMC, in green) joined to a nitroacenaphathenequinone (NANQ, in red) fluorophore by means of a six-carbon linker (in black) that fits in COX-2 (see Scheme 1).

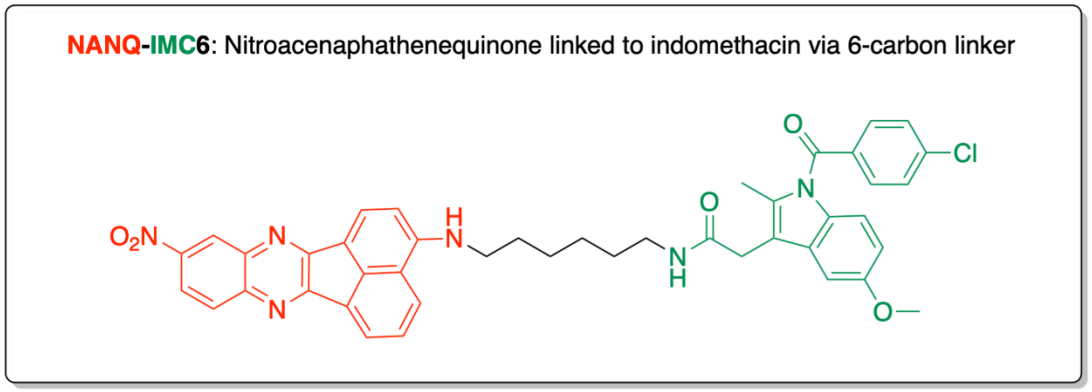

Scheme 1: COX-2-specific fluorogenic probe NANQ-IMC6.

NANQ-IMC6 under two near-infrared photon excitation at 800 nm is nonfluorescent in the absence of COX-2 in solution (where it adopts a folded conformation), but its fluorescence is "turned on" in both mice inflammatory lesions and tumor tissues. Surprisingly, the fluorescent emission turns out to be quite different at these two sites: The cancerous tissues show a strong fluorescence signal in the green channel (emission peak at 555 nm), while inflammatory tissues revealed an image in the red channel (emission peak at 615 nm). In that study (Zhang et al., 2013), the authors hypothesized that this spectral shift is a consequence of the highly different concentrations of COX-2 in the two cases: COX-2 in inflammatory lesions (and in normal cells with constitutive COX-2 as well) would be present as a monomer, whereas it would exist as a homodimer when it is overexpressed at high concentrations in tumor tissues. The possibility that COX-2 is present as a homodimer only in cancer tissues, but a monomer elsewhere, would open a new promising strategy to rationally design novel drugs that selectively inhibit the COX-2 homodimer in cancer, but without affecting the constitutive COX-2 monomer, thus avoiding the above-mentioned harmful side effects.

Therefore, it is of interest to assess the dimerization hypothesis and rationalize the molecular basis of the changes in NSAID binding upon dimerization that lead to such a fluorescence shift. In this paper, we present a first-principles multiscale simulation protocol to inspect the impact of dimerization on the fluorescence properties of NANQ-IMC6. Our approach combines ground state molecular mechanics molecular dynamics (MM-MD), multiple excited state adiabatic QM/MM Born-Oppenheimer MD (BOMD) simulations, and postprocessing of these trajectories with polarizable embedding QM/MMPol calculations based on time-dependent density functional theory (TD-DFT). (Curutchet et al., 2009; Ozaydin & Curutchet, 2023) QM/MM adiabatic and non-adiabatic multiple excited state dynamics have emerged as a powerful tool to investigate the

photochemistry and spectroscopy of biological systems. (Brunk & Rothlisberger, 2015; Crespo-Otero & Barbatti, 2018; Nelson et al., 2020; Nottoli et al., 2023) For example, non-adiabatic approaches have been extensively used to shed light into the photoactivation of rhodopsin (Groenhof et al., 2020), and adiabatic methods have been applied to tackle the proton-coupled electron transfers that characterize photoactivation of the blue-light-using flavin domain of the AppA protein. (Mazzeo et al., 2023) Here, we apply adiabatic simulations and polarizable embedding to simulate the fluorescence spectra of the COX-2-specific fluorogenic probe NANQ-IMC6 in models of complexes of this probe with a human COX-2 (hCOX-2) monomer and homodimer. Our findings indicate that the emission shift arises from dimerization of the highly overexpressed COX-2 in cancer tissues and suggest that the spectral shift is linked to changes in specific electrostatic protein-probe interactions upon dimerization due to resulting changes in the environment of the probe. In contrast, the role of steric effects related to modulation of the NANQ geometry by the protein scaffold in each situation are found to be minor and even leading to an opposite small shift.

2. Results & Discussion

We started by docking the NANQ-IMC6 ligand in the active sites of the hCOX-2 monomer (from now on named as single monomer) and dimer. As seen in Scheme 1, NANQ-IMC6 contains a large alkyl chain with multiple rotatable bonds, thus having a large degree of conformational flexibility. The scaffold of the NANQ chromophoric moiety is a large planar and rigid structure, which clearly cannot fit inside the COX-2 cavity. This suggests that only the IMC unit interacts with the residues of the active site, and the 6-carbon chain connects the two moieties inside and outside the binding pocket. As the structure of the single monomer was taken from the first monomer (A) of the homodimer crystal, the same docking was used in these two cases, whereas the ligand was docked again for the second monomer (B) of the homodimer. Because the docking was done with a rigid protein, the adoption of the monomer A structure for the single monomer at this point does not pose any inconvenience. Figure S1 shows the binding mode of NANQ-IMC6 in the active site of monomer A obtained from the first ranked docking solution, once a clash has been eliminated. Since initially the monomers are identical, the binding mode for monomer B is the same. As discussed above, Figure S1 shows that the IMC6 part of the molecule remains inside the active site. In contrast, the NANQ part is found outside. In hCOX-2, the residues Arg-120, Tyr-355, and Glu-524 form a constriction that must open to provide access into the active site. These three residues define the top of a spacious alcove (called the lobby) surrounded by the four helices of the membrane-binding domain. (Rouzer & Marnett, 2020) In the crystal structure of the complex COX-2:indomethacin (Kurumbail et al.,1996), the carboxylate group of indomethacin interacts with the hydrogen atoms of Arg120. That carboxylate group does not longer exist in the IMC part of the NANQ-IMC6 construct, as it becomes an amide group, but the carbonyl nevertheless maintains the interaction with the Arg120.

Starting from the refined docking structure, we carried out a 500 ns MM-MD simulation at 298.15K on the ground state potential energy surface for the hCOX-2 monomer and homodimer. The root-mean-square deviation (RMSD) of NANQ-IMC6 along the single monomer simulation, shown in Figure S2, clearly shows the stability of the complex. After an initial increase in RMSD, the ligand displays rather small structural fluctuations, the initial jump appearing as the ligand accommodates the binding mode predicted by docking. On the other hand, the simulation of the homodimer shows different behaviours

for monomers A and B. The RMSD of the ligand in monomer A, shown in Figure S3, resembles that of the monomer in Figure S2. However, in monomer B there is a larger change in RMSD (see Figure S4), arising from a larger readjustment of the initial docking pose. In this case, this structural rearrangement however lasts almost 100 ns, and involves a displacement of the ligand outside of the cavity. To compare this behavior in monomers A and B, Figures S5 and S6 show the distances between the ligand and the center of mass of Arg120 (part of the door of the active site) along the trajectory. In monomer B, the distance increases up to 22 Å, in contrast to a maximum value of 12 Å in monomer A. Thus, the structural reaccomodation of the ligand in the two monomers is quite asymmetric. In monomer A the ligand behaviour resembles that in the COX-2 single monomer, but in monomer B it tends to move far away from Arg120, as illustrated by the last MM-MD frames shown in Figures S7, S8 and S9. In all cases, the NANQ moiety is beyond the Arg120 and Tyr355 door. The carbon linker is inside the active site in monomer A, but outside in monomer B and the single monomer. Protein-ligand binding takes place through hydrogen bond interactions between the IMC moiety (always inside the active site) and some COX-2 residues whose identity depends on each case. To get more insights in the differences between the two monomers of the homodimer, a root-mean-square-fluctuation (RMSF) analysis was done. Figure S10 shows how the residues involved in monomer A displayed smaller movements along the simulation in comparison with the residues in monomer B. Overall, this analysis indicates that the configurations explored by the single monomer or monomer A of the homodimer are significantly different to those in monomer B. It is interesting to highlight that the IMC moiety of the ligand occupies the same region inside the cavity in the three cases (although the three structures are far from matching), whereas the NANQ moiety, which is quite free outside the cavity, shows considerable heterogeneity, appearing the ligand in monomer B particularly different compared to the other two cases, as shown in Figure 1.

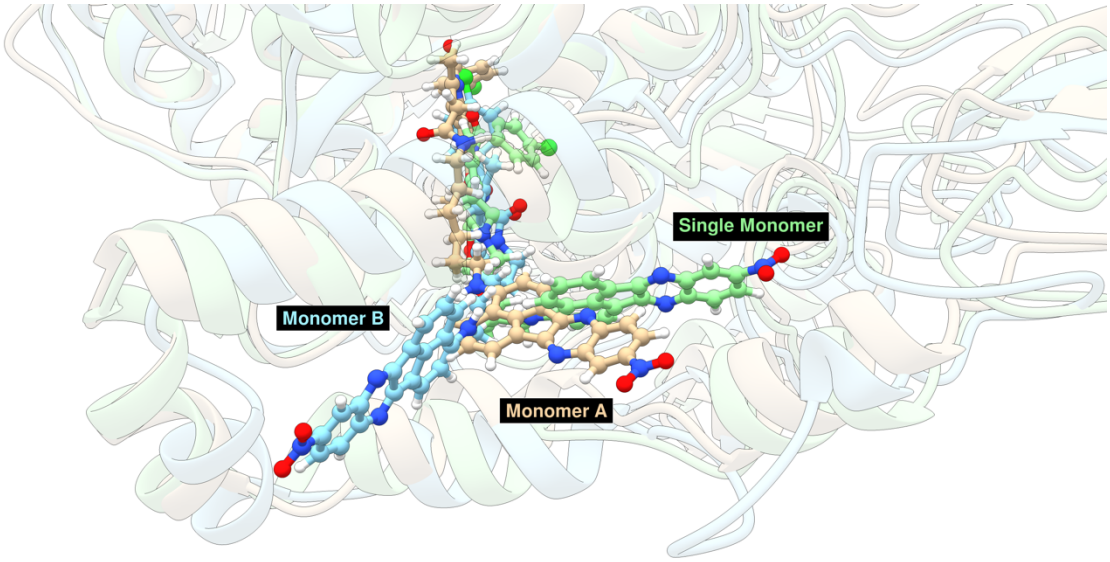

Figure 1. Superposition of the configurations adopted by NANQ-IMC6 in the last frame of the MM-MD trajectories. The colors light green, tan and light blue correspond to the single monomer, monomer A of the homodimer, and monomer B of the homodimer of hCOX-2.

To simulate the fluorescence arising from this heterogenous arrangements of NANQ outside the binding site, we then run multiple adiabatic QM/MM BOMD simulations to sample the configurational space of the S_1 emitting excited state starting from different

configurations extracted from the MM-MD trajectory. Before this, we inspected the energy difference between the first (S_1) and second (S_2) excited states, to gauge the probability of eventual nonadiabatic transition between them mediated by structural fluctuations in the real system.

We also assessed the transition dipole moments and oscillator strengths of the S_1 and S_2 states, to identify the lowest bright excited state expected to fluoresce according to Kasha's rule. (Braslavsky, 2007) In Table S1, we report preliminary calculations performed on the optimized gas-phase geometry of unfolded NANQ-IMC6 performed at the TD-B3LYP/6-31G(d) level of theory (note that although unbound NANQ-IMC6 exists mainly in its folded form,[7] we are interested here in the fluorescence arising from the unfolded structure that adopts inside COX-2). The results indicate that S_1 is about 0.3 eV below S_2. This would support the suitability of adiabatic QM/MM BOMD simulations on S_1 in gas phase. Moreover, the electronic transition dipole moment and oscillator strength (0.25) of S_1 are significant, indicating that this state is directly populated upon absorption and is expected to generate the fluorescence signal. On the other hand, Figures S11, S12 and S1 report the HOMO, LUMO and LUMO+1 molecular orbitals of unfolded NANQ-IMC6 in gas phase. These orbitals are fully located on the NANQ scaffold, the fluorophore part of the ligand, thus supporting the fact that excitations involving these orbitals, as shown in Table S1, are those corresponding to the fluorescence band.

To carry out the adiabatic BOMD simulations on S_1, we started from 10 equally spaced snapshots extracted from each of the two MM-MD simulations (single monomer and homodimer). In all BOMDs, the NANQ unit of a single ligand (in red in Scheme 1) was included in the QM region. For the homodimer, 10 simulations were carried out considering the NANQ in monomer A in the QM region, and another 10 for the ligand in monomer B in the QM region. These calculations were done independently for NANQ-IMC6 in monomer A and B, as the distance between them (beyond 30 Å), each one located in its respective cavity, prevent significant excitonic interactions between them. Beyond the exploratory calculations in gas-phase reported above, we also investigated the energy difference between the three lowest-energy excited states along a 150 fs BOMD simulation of the single monomer, using different DFT functionals, as reported in the computational details. Results showed similar trends in all cases, with M06 providing a slightly larger energy difference between S_1 and S_2 compared to B3LYP (see Figure S14). We thus selected the TD-M06/6-31G level of theory for the BOMD, as it keeps a large energy gap between the S_1 and S_2 states, thus justifying the adequacy of the adiabatic treatment.

Then, in order to account for environmental polarization effects, we postprocessed the BOMD frames with polarizable embedding calculations at the TD-M06/6-31G(d)/MMPol level of theory. We then simulated the fluorescence spectra, which are shown in Figures 2 and 3, both using a stick spectrum, or by accounting for the missing broadening convoluting the sticks with a Gaussian function. Despite their attractive cost-quality ratio, TD-DFT methods provide errors in the range ~0.2-0.4 eV (Loos et al., 2020), depending on the functional chosen. To correct for that systematic error, we shifted all energies by +0.51 eV to match the emission maxima in the simulated Gaussian-broadened spectra with the experimental maximum observed for the monomer at 615 nm, resulting in the spectra shown in Figures 2 and 3. Furthermore, we removed the first classical 100 ns of monomer B of the homodimer in order to only reproduce the realistic

binding mode of monomer B (see below). The simulated spectra of the complex indicate maxima for the monomer and dimer at 615 nm and 540 nm (Figure 3b), with a dimerization hypsochromic shift of -75 nm (+0.28 eV), in good agreement with the experimental observed shift of -60 nm (+0.22 eV) (Zhang et al., 2013). Note, however, that before applying the systematic correction for M06, the gaussian-convoluted emission maxima were found at 731 nm and 627 nm for the monomer and dimer, respectively, leading to a -104 nm shift.
In order to dissect the origin of the fluorescence shift upon dimerization, we then recomputed the TD-M06 excitation energies along BOMD trajectories by deleting the protein and solvent environment and only keeping the NANQ-IMC6 ligand, in order to gauge how internal geometry fluctuations of NANQ in the monomer and the dimer impact the emission compared to specific electrostatic and polarization specific NANQ-protein interactions. In Figures 2a and 2b we report the stick and fluorescence spectra of the monomer and the homodimer computed in vacuum, which can be compared to the spectra of the monomer and the homodimer in the complete solvated complex (Figures 3a and 3b). For the complete system, the maxima of the monomer and homodimer are found at 615 nm and 540 nm (586 nm and 500 nm in the stick spectrum), respectively. In contrast, in vacuum the maxima of the monomer and dimer are found at 406 nm and 410 nm (389 nm and 394 nm for the stick spectrum). Thus, the geometrical constraints imposed to NANQ-IMC6 in the monomer and homodimer complex indeed lead to a dimerization bathochromic red shift of +4 nm (-0.03 eV), with the opposite sign compared to the shift imposed by electrostatic interactions. This indicates that the specific interactions of NANQ-IMC6 with COX-2 and the surrounding waters are responsible for the opposite hypsochromic shift experimentally observed.

To validate the data from Figures 2 and 3, TD-DFT QM/MMPol calculations along the BOMDs were also performed using the range-separated CAM-B3LYP hybrid functional, as shown in Figure S15. The fluorescence changes between the monomer and the homodimer are very similar to those found using M06. Thus, despite the fact that the excited states have some degree of charge transfer, as illustrated by the molecular orbitals characterizing S_1 shown in Figures S11, S12 and S13, our results seem to be robust toward the choice of the DFT functional describing the excited state.

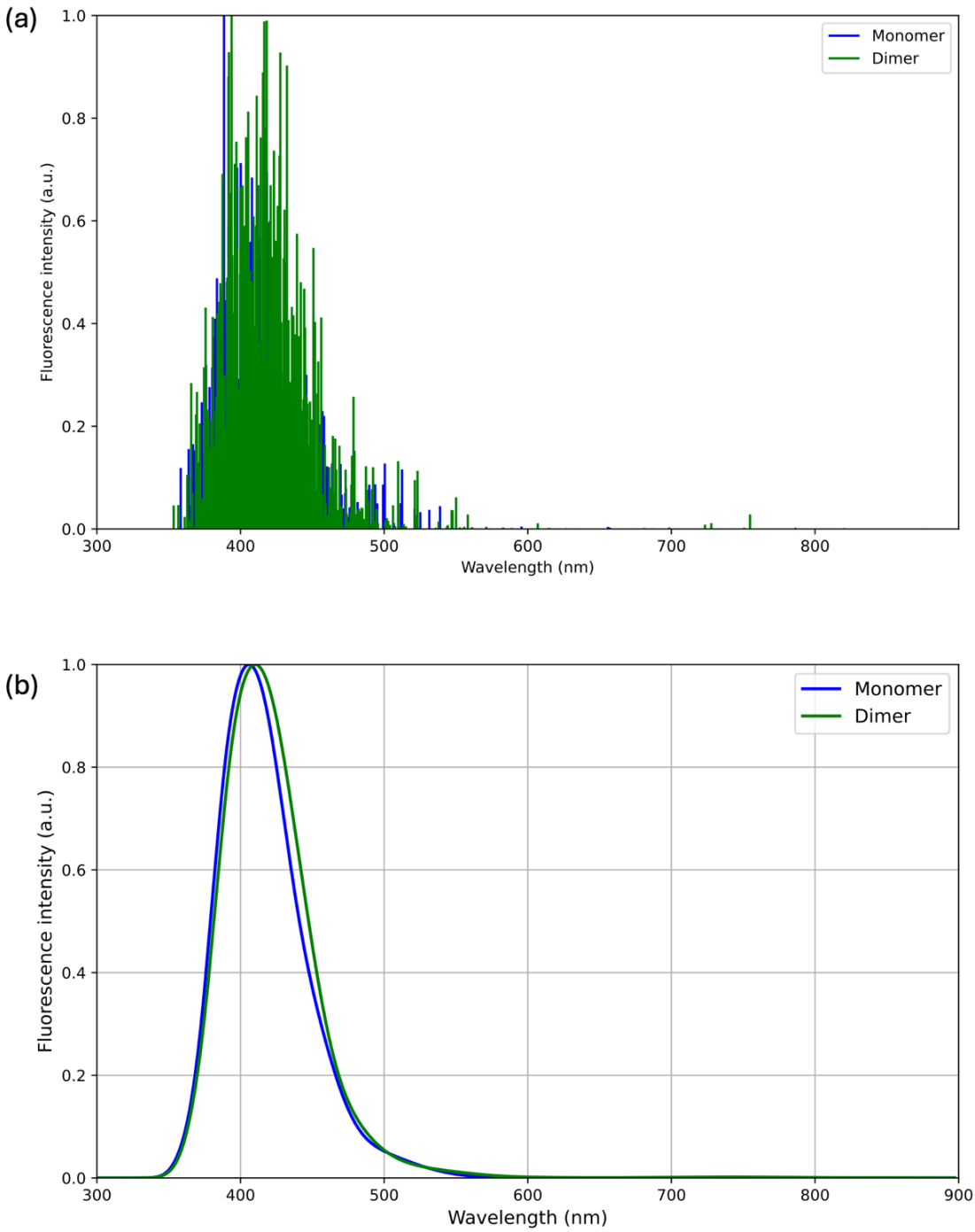

Figure 2. (a) Fluorescence stick spectra and (b) gaussian-convoluted fluorescence spectra of NANQ-IMC6 in vacuum computed from geometries extracted from excited state BOMD simulations of the complete hCOX-2:NANQ-IMC6 single monomer and homodimer complexes. In homodimer spectra, NANQ moieties of the ligand bound to monomer A and monomer B contribute equally. All spectra simulated from TD-M06/6-31G(d)/MMPol excited state calculations. All energies are shifted by +0.51 eV (see text).

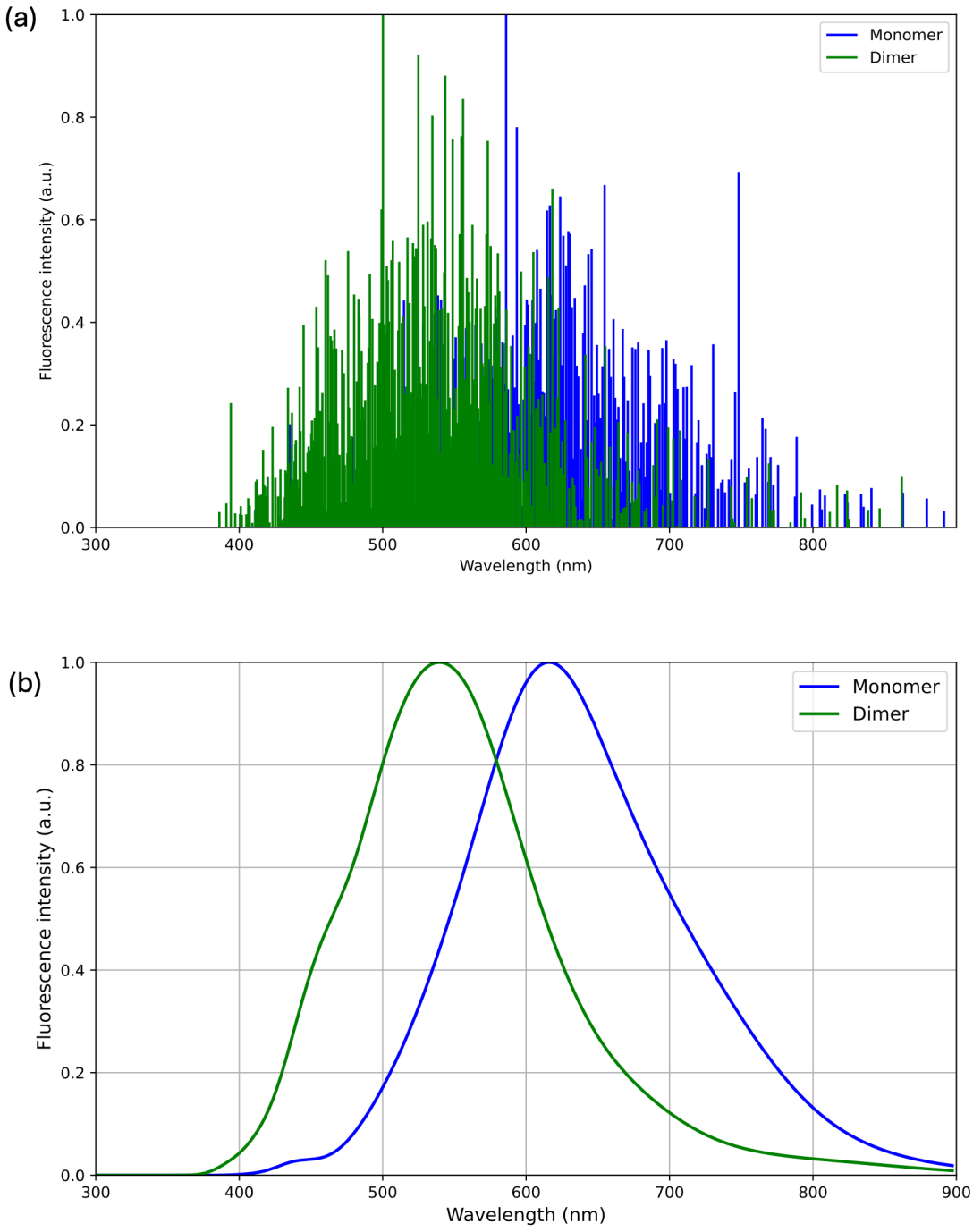

Figure 3. (a) Fluorescence stick spectra and (b) gaussian-convoluted fluorescence spectra of NANQ-IMC6 for the complete hCOX-2:NANQ-IMC6 single monomer and homodimer complexes computed from geometries extracted from the corresponding excited state BOMD simulations. In homodimer spectra, NANQ moieties of the ligand bound to monomer A and monomer B contribute equally. All spectra simulated from TD-M06/6-31G(d)/MMPol excited state calculations. All energies are shifted by +0.51 eV (see text).

Our results thus support that the highly overexpressed COX-2 in cancer cells exists as a homodimer, whereas COX-2 is present in inflammatory lesions as a monomer. The question then arises on what the molecular basis for the fluorescence spectral changes

upon dimerization is. Zhang et al. (2013) have hypothesized that the fluorogenic moiety NANQ has a hydrophilic environment in the single monomer, but it penetrates in the large hydrophobic channel corresponding to the monomer A:monomer B interface in the homodimer. This would affect the stabilization of the electron density transferred from the amino part of NANQ to the nitro group due to the electronic excitation. In effect, we have calculated the excitation wavelength to the first excited state (S_1) of the NANQ fluorophore in three different solvents using the IEFPCM continuum solvation model (Table S2). Figures S11 and S12 confirm a remarkable transfer of electronic density to the nitro group upon excitation, whose stabilization increases with solvent polarity as the dielectric constant is larger, leading to a larger excitation wavelength.

However, our simulations indicate that the ligand NANQ-IMC6, with the IMC moiety in the binding site of COX-2, is too short for the fluorophore NANQ to reach the hydrophobic monomer A:monomer B interface in the homodimer. In contrast, we have analysed the surroundings of the nitro group in the MM-MD simulations of the single monomer and the homodimer. Comparing Figures 4a and 4b, we see that the access of water molecules to the oxygens of the nitro group is quite free in the monomer, whereas Lys78 somewhat hinders the close interaction water-nitro group in the monomer A of the homodimer. A more complete view of this change in hydration pattern can be obtained comparing the water radial distribution functions around one of the oxygen atoms of the nitro group in the MM-MD simulations of the monomer and the homodimer, and the corresponding integrated water radial distribution functions, as shown in Figures 4c and 4d. The water access at short distances is slightly better in the case of the single monomer than in the case of the two monomers of the homodimer. This difference is enough to lower the energy of the S_1 state of the ligand in the monomer more than in the case of the homodimer, thus leading to the bathochromic shift in the monomer.

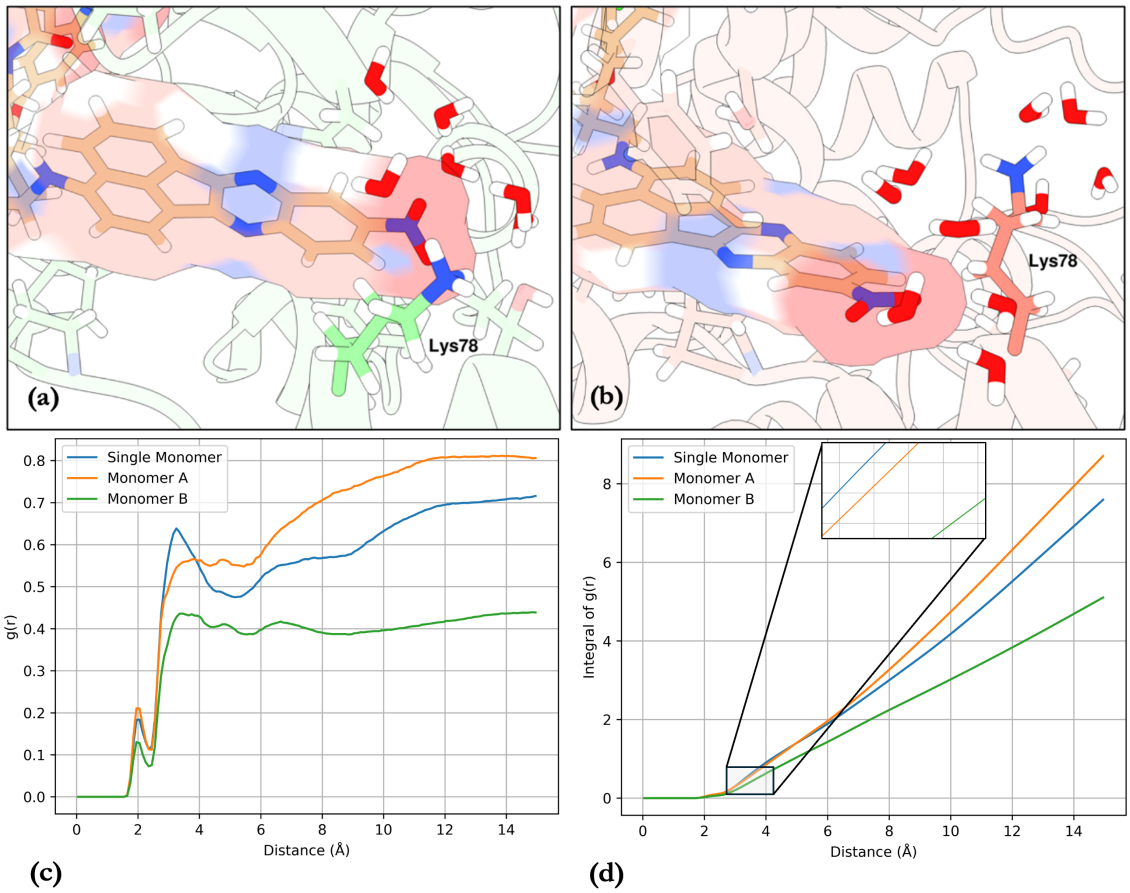

Figure 4. (a) View of the surroundings of the nitro group in the last frame of the MM-MD simulation of the single monomer; (b) View of the surroundings of the nitro group in the monomer A in the last frame of the MM-MD simulation of the homodimer; (c) Water radial distribution functions around one of the oxygen atoms of the nitro group in the MM-MD simulations of the single monomer and the homodimer; (d) Corresponding integrated water radial distribution functions.

Related to the previous analysis on water hydration of the different molecules, the question is why this is happening. In Figures 1, 4 and 5 we illustrate the binding modes of the ligands in the single monomer and the homodimer. It seems clear that changes in water accessibility, as well as differences in the NANQ-protein specific interactions, for example with Lys78, are responsible for the observed hypsochromic shift upon dimerization. As discussed previously, this shift could also be partially due to different structural deformations experienced by the NANQ moiety in the monomer and homodimer complexes, or by changes in flexibility, which can be estimated by the degree of structural fluctuations. In particular, distortion of the NANQ planarity is expected to impact the π-π* excitation energies, as it commonly occurs in the biological function of tetrapyrrole pigments, for example chlorophylls in light-harvesting complexes. (Senge et al., 2015; Lahav et al., 2021; De Vico et al., 2018) In Figure 5a we illustrate the structural flexibility of NANQ-IMC6 in the single monomer and monomers A and B in the dimer from excited state BOMD simulations used in QM/MMPol calculations of the fluorescence spectra. This Figure clearly shows that NANQ has less conformational freedom in the binding site of the single monomer compared to those in the dimer. It was prepared by drawing a representative subset of frames extracted from the excited state BOMD trajectories used to simulate the fluorescence spectra reported in Figures 2 and 3, so that they illustrate the heterogeneity of conformations contributing to the emission. On

the other hand, in Figure 4b we depict the progressive displacement of NANQ-IMC6 in monomer B along the MM-MD simulation from an open to a closed configuration (see the fast RMSD change between 50 ns and 100 ns simulation in Figure S4). It is possible to observe how a loop and an α-helix contribute to the modification of the binding mode of NANQ-IMC6 in monomer B, which remains quite stable from 100 ns. This rearrangement does not occur in monomer A (see the stable RMSD for 500 ns in Figure S3), leading to a difference in the behavior of each monomer. Hence, this difference challenges the view of COX-2 as a homodimer. This binding mode change does not happen either along the 500 ns MM-MD simulation of the single monomer (see RMSD in Figure S2), where the intermonomer interaction is lacking. See Figures S16 and S17 to compare the behaviours of the single monomer and the two monomers in the dimer.

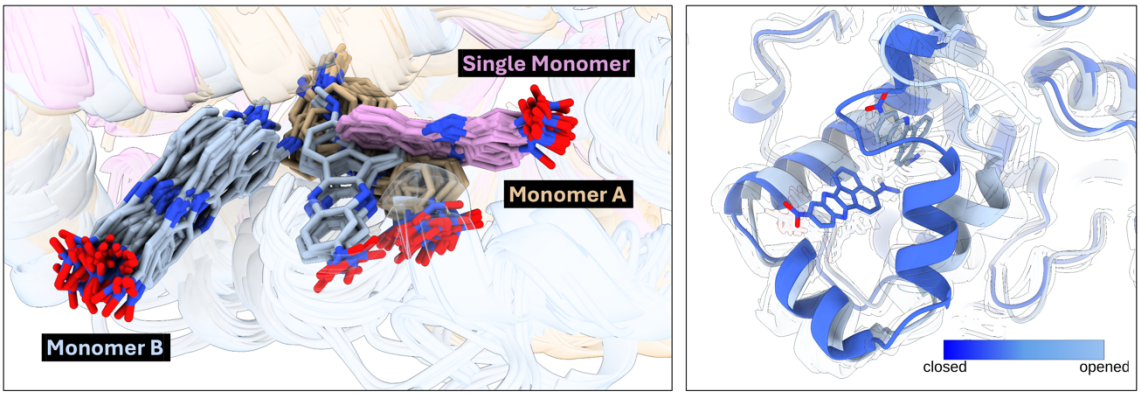

Figure 5. (a) Comparison of a representative subset of structures extracted for the single monomer (pink) and the monomer A (tan) and monomer B (blue) of the dimer from excited state BOMD simulations used in QM/MMPol calculations of the fluorescence spectra. **(b)** Displacement of NANQ-IMC6 in monomer B due to the movement of a loop and an α-helix (open to closed) towards the molecule (initial frames in light blue; final frames in royal blue) occurring along the MM-MD trajectory.

Thus, an intriguing point is why the position of the ligands in both monomers A and B in the homodimer are different. It has been proposed (Yuan et al., 2006; Smith & Malkowski, 2019) that COX-2 homodimers function as conformational heterodimers having allosteric and catalytic subunits. Thus, binding of a ligand to the COX-2 site of one monomer would alter its companion monomer, as observed in Figure 5b. The movement of the loop and the α-helix in monomer B leads to a modification of the binding mode of NANQ-IMC6. This is probably related to the uncertain heterodimer functionality of the enzyme. It is not clear how the crosstalk between both monomers takes place. Although both ligands are too far to directly interact, as shown in Figure S18 (up to 33 Å separation), we have used the webPSN, based on mixed Protein Structure Network and Elastic Network Model-Normal Mode Analysis. (Felline et al., 2020) server to investigate the allosteric structural communication between the two NANQ-IMC6 ligands (Figure 6) through the enzyme. The results indicate that structural communication from monomer A to monomer B follows a path of interactions through the homodimer, crossing the large hydrophobic site pocket (easily recognized in Figure 6). The interaction strength is high along the red path, with a part of the communication path with a cross-correlation of atomic motions somewhat less strong (indicated in blue). Thus, the presence of a ligand in monomer A can influence the binding of the other in monomer B.

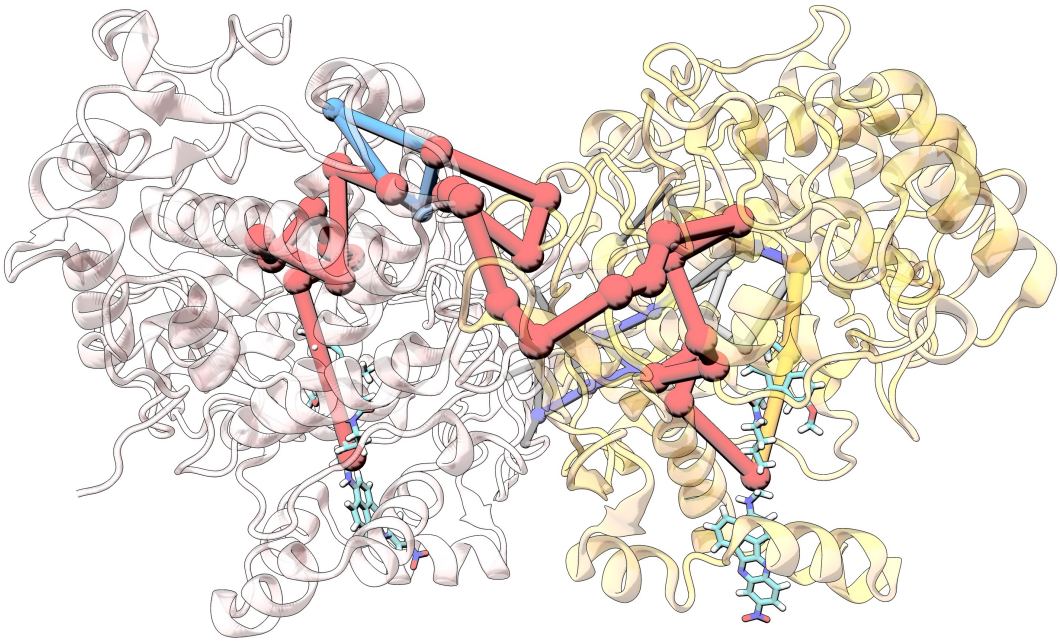

Figure 6. Allosteric communication path predicted by the webPSN server between the NANQ-IMC6 ligands in monomer A and monomer B of the homodimer of hCOX-2.

To get a deeper insight into the contributions of the enzyme and the water environment to the shift of the fluorescence spectra upon dimerization we have depicted the spectra of NANQ-IMC6 in vacuum (Figure S19), excluding waters (Figure S20), and for the complete hCOX-2:NANQ-IMC6 single monomer and homodimer complexes (Figure S21), including in all cases the contributions of each monomer (A and B) to the dimer spectra, and computed from geometries extracted from excited state BOMD simulations of the complete hCOX-2:NANQ-IMC6 single monomer and homodimer complexes. As in Figure 2b, Figure S19 (in vacuum) shows a slight bathochromic red shift upon dimerization, with very similar contributions corresponding to monomer A and B in the dimer. These results account for the different geometries adopted by NANQ-IMC6 in the different situations. When the effect of the electrostatic interactions with the enzyme is added in Figure S20, all the spectra are moved to longer wavelengths (this red shift increases in the order monomer B in the dimer < dimer < monomer A in the dimer < single monomer), and then some hypsochromic blue shift already appears upon dimerization. Interestingly, that read shift is clearly smaller for the case of the monomer B of the dimer because the quite charged nitro group of NANQ-IMC6 is close to non-polar residues (for instance, two valines) in monomer B, but has several polar residues (for instance, two lysines and one tyrosine) in monomer A, then the electrostatic interaction in S_1 is bigger in this second case. Indeed, the spectrum corresponding to the complete dimer is intermediate to the spectra corresponding to its two monomers. The most important change occurs when the effect of the electrostatic interactions with the water solvent is added in Figure S21, where the three effects (geometric, enzyme and water solvent) are included. Now, the displacement of the spectra towards longer wavelengths is bigger than that produced by the interaction with the enzyme, especially for the case of the single monomer, with a red shift due to water solvent of +143 nm (the smaller red shift corresponds to the monomer B of the dimer, +69 nm due to water solvent, versus +95 nm for the monomer A of the dimer). As a consequence, the experimental hypsochromic blue shift upon dimerization clearly appears in Figure S21 and can be fundamentally attributed to the differential water solvation in the single monomer and in the dimer. As mentioned previously (see Figure 4), the access of the water solvation is

more important in the single monomer than in the monomers of the dimer. As also seen in Figure S22, the lower accessibility of water to NANQ-IMC6 (and its nitro group) in monomer B than in monomer A of the dimer produces a quite smaller red shift for monomer B upon water solvation (compare Figures S20 and S21).

Finally, after analyzing in detail the energetic behavior of monomers A and B of the homodimer separately, we have been able to see the effect of the two different binding modes of monomer B producing different maximum intensities. As graphed in Figure S23, when the first 100 ns on the spectrum of monomer B are included, it is possible to observe a second maxima for monomer B around 550 nm. This value is quite similar to the maximum observed for monomer A. Along these first 100 ns monomer B adopts an open configuration comparable with the one corresponding to monomer A, and with a similar water accessibility for NANQ-IM6. From 100 ns to 500 ns monomer B maintains a closed configuration (see Figures 4, S16 and S17) that produces its first maximum at 484 nm. Since the fast evolution of monomer B is caused by the intermonomer interaction, we have considered that the fluorescence spectrum is recorded experimentally when monomer B is already in its closed configuration. Thus, for the calculation of the spectra we have removed throughout this paper the first classical 100 ns of monomer B of the homodimer in order to only reproduce the realistic binding mode (closed) of monomer B. Anyway, the inclusion of those first 100 ns (that is, open + closed configurations of monomer B) would show a hypsocromic blue shift of -66 nm upon dimerization (Figure S23), still in very good agreement with the experimental spectra.

3. Conclusions

We reported a first-principles study of the molecular basis of the fluorescence spectra in complexes between NANQ-IMC6 and monomeric and homodimeric forms of the human COX-2 enzyme. We employed a multiscale protocol that combines extended MM-MD simulations with short multiple excited state adiabatic QM/MM BOMD simulations, which allows to account for both protein conformational heterogeneity at the ground state and multiple protein reorganization events after ligand photoexcitation. All our simulated spectra indicate an hypsochromic shift upon dimerization, in good agreement with experiments. In particular, the gaussian-convoluted corrected hypsochromic blue shift is -75 nm (+0.28 eV). We find that this effect entirely arises from changes in electrostatic interactions between NANQ and the protein and water environment, in particular due to the slightly greater water accessibility to the nitro group of the fluorogenic moiety in the case of the monomer. In contrast, the impact of the deformation of the planarity of the π system of NANQ, estimated by recomputing the spectra from vacuum calculations performed using NANQ-IMC6 geometries extracted from the protein-ligand complex trajectories, is found to be small, leading to an opposite bathochromic red shift of +4 nm (+0.03 eV). Our results thus support that the highly overexpressed COX-2 in cancer tissues is present as a homodimer, in contrast to the monomer structure adopted in inflammatory lesions and, evidently, in constitutive COX-2. Our findings thus pave the way for the rational design of new anti-inflammatory drugs to treat cancer efficiently by selectively inhibiting the homodimer of COX-2, thus minimizing undesired harmful side effects. In addition, it demonstrates the potential of first-principles simulations in the design of specific fluorogenic probes able to shed light on the formation of protein multimers and monitor other structural transitions in proteins.

4. Computational methods

4.1. System setup. The structure of the human COX-2 homodimer system was obtained from the crystal of salicylate-bound human COX-2 (PDB entry 5F1A) and cleaned deleting salicylate, waters, and other molecules. Since the reactive residue Tyr385 is almost certainly found as a tyrosyl radical (Cebrián-Prats et al., 2019), we eliminated the hydrogen atom of the hydroxyl group of this tyrosine residue. Hydrogens topology for all the other residues of the structure were generated with the H++ web-server (Gordon et al., 2005; Anandakrishnan et al., 2012) using a pH = 7.4 for titratable residues. The COX-2 single monomer system was then obtained by deleting one of the monomers in the homodimer.

4.2. Molecular docking. Starting from the structures generated from the crystal, docking calculations were done to insert the NANQ-IMC6 ligand in the active site of the monomeric and homodimeric human COX-2. We employed the program AutoDock Vina. (Trott & Olson, 2010) In these calculations the receptor was kept fixed, whereas the ligand was completely flexible to be docked in the cavity. The binding site cavity used in the docking runs was a 20Å × 20Å × 20Å squared box centred at the Val523 residue for the first monomer, and at the Val1107 residue for the second monomer. In practice, however, given that two ligands should be bound in the homodimer structure, the docking was performed in two steps. A first ligand was docked in the empty enzyme structure and, subsequently, the second ligand was docked in the other monomer.

4.3. Parameterization. The ferric penta-coordinate high spin group (Fe^{3+}) atomic charges were obtained from a calculation with the RESP[24] method at the HF/6-31G(d,p) level of theory, and parameters for the heme group were taken from the literature. (Shahrokh et al., 2012) Axial histidine parameters are well-described by the general AMBER force field GAFF. (Wang et al., 2004) The tyrosyl radical parameterization was done in previous studies by Cebrián-Prats, et al. (2019) optimizing the residue with the B3LYP (Lee et al., 1988; Becke, 1993) functional and the 6-31G(d,p) basis set and calculating the partial atomic charges by using the RESP (Bayly et al., 1993) method in AmberTools using the ESP computed with Gaussian09 (Frisch et al., 2009). The NANQ-IMC6 parameterization was done in this work at the same level of theory as used for the tyrosyl radical using Gaussian16 (Frisch et al., 2016) and employing the GAFF force field. Finally, the force field ff19SB (Tian et al., 2020) was used for the rest of the protein.

4.4. Classical ground and excited state MD simulations. After the setup up and force field parameterization, the systems (single monomer and homodimer, including the corresponding ligands and OPC (Izadi et al., 2014) water box) were minimized using the steepest descent and conjugate gradient methods on a MM ground state potential energy surface. Three steps applying restraints on ligands, heme group and enzyme were carried out. The last minimization step was done with no restraints. Afterwards, a molecular dynamics simulation was done on this potential energy surface (MM-MD). Firstly, the systems were heated from 0K to 300K in the NVT ensemble under periodic boundary conditions. Then, an MM-MD simulation in the NPT ensemble was performed during 5 ns to equilibrate the density of the systems at 298.15 K. Next, from the final structures of the previous simulations, taking the volume corresponding to 1 atm, an equilibration of 10 ns in the NVT ensemble was performed. Finally, the production phase was carried out for 500 ns to ensure enough sampling. These MD simulations were carried out using the

Amber20 (Case et al., 2020) software with a time step of 1 fs, freezing hydrogen bonds with the SHAKE algorithm, and using the force fields indicated in section 4.3.
In addition, adiabatic QM/MM Born-Oppenheimer Molecular Dynamics (BOMD) were run for a total of 3 ps of simulation: 1 ps in the ground state followed by 2 ps in the first electronic adiabatic excited state (S_1) using TD-DFT and a time step of 0.5 fs. Exploratory simulations were performed using the B3LYP, CAM-B3LYP, M06 and ωB97XD functionals, as well as the *ab initio* CI-Singles (CIS) method, using the 6-31G basis set, whereas production runs were based on the M06 functional. The simulations were done on a QM/MM potential energy surface calculated at every step by connecting Amber20 (Case et al., 2020) and Gaussian16 (Frisch et al., 2016) through the interface available in Amber to perform this type of simulations. Multiple BOMD replicates of sufficient length (see above) to ensure adequate sampling were started from 10 equally spaced frames extracted from the same MM-MD production simulation. For the monomer structure, the NANQ part of the compound (in red in Scheme 1) was included in the QM region (36 atoms of a total of 9030 protein-ligand atoms and 19666 water molecules). For the case of the homodimer, 10 replicates were carried out considering the NANQ moiety of the ligand in monomer A in the QM region, and another 10 replicates (starting from the same initial structures) were carried out considering the NANQ moiety of the ligand in monomer B in the QM region (36 atoms of a total of 18048 protein-ligand atoms and 31549 water molecules). A scheme of the overall classical (ground and excited state) MD simulation protocol is presented in Figure S24. One link atom was employed between the N-QM atom of NANQ and the first carbon atom of the linker.

4.5. Vacuum and continuum solvent excited state calculations. Exploratory TD-DFT calculations were performed for NANQ-IMC6 (73 atoms) based on its unfolded geometry optimized at the TD-B3LYP/6-31G(d) level of theory in gas phase. The first three low-lying singlet excited states of the molecule were analysed to characterize and verify that the first excited state (S_1) is the one responsible of the fluorescence. Test calculations were then performed on NANQ using the IEFPCM continuum solvation model from TD-DFT and geometry optimizations performed at the CAM-B3LYP/6-31G and M06/6-31G level of theory to explore the impact of different solvents (dichloromethane, methanol, water) on the emission properties.

4.6. QM/MMPol excited state calculations and fluorescence spectra. The fluorescence properties of NANQ-IMC6 bound to human COX-2 (monomer and homodimer) were then calculated using polarizable embedding linear response TD-DFT calculations based on the MMPol (Curutchet et al., 2009) model performed at the TD-M06/6-31G(d) level of theory. The protein MMPol environment was described using the Amber pol12 AL polarizable force field (Wang et al., 2011a; Wang et al., 2011b), the atomic polarizability for Fe^{3+}, not defined in pol12, was derived from a B3LYP/aug-cc-pVTZ calculation, MMPol parameters for water were taken from previous work (Corbella et al., 2019), and polarization-consistent ESP charges for the heme group, axial histidine, the tyrosyl radical and NANQ-ICM6 were obtained using the Polchat tool (Caprasecca et al., 2014) from ESPs computed at the HF/6-31G(d) level of theory. Explicit polarization was limited to residues within a cutoff radius of 15 Å from the QM heavy atoms (MMPol region), whereas residues up to a 30 Å were also included but adopting the additive force field (MM region) used in the MD. All QM/MMPol calculations were carried out using a locally modified development version of Gaussian. (Frisch et al., 2010) For the monomer, fluorescence was modelled from QM/MMPol data computed for 100 structures extracted from the last ps of each of the 10 S_1 BOMD trajectories reported above considering

NANQ in the QM region. For the homodimer, 50 structures were similarly extracted from each BOMD simulation with NANQ in monomer A and 50 structures with NANQ in monomer B (see Figure S17). In addition, the robustness of the results was also investigated by recomputing the excitation energies at the QM/MMPol TD-CAM-B3LYP/6-31G(d) level of theory. The normalized fluorescence spectra were modelled as stick spectra proportional to the squared electronic transition dipole moments (S_1 to S_0) using a 2 meV bin, each stick representing a QM/MMPol excited state TD-M06/6-31G(d) calculation performed along the BOMD trajectories. Then, a more realistic spectrum was constructed by convoluting each stick with a gaussian function with a FWHM of 200 meV. Systematic errors associated to specific functionals were corrected by shifting all vacuum QM and protein QM/MMPol excitation energies by +0.51 eV (M06) and -0.20 eV (CAM-B3LYP) to reproduce the experimental maximum at 615 nm observed for the monomer in the gaussian-convoluted spectrum.

Acknowledgments
This work was supported by the "Ministerio de Ciencia, Innovación y Universidades" of Spain through projects PID2020-113764GBI00, PID2020-115812GB-I00 and CEX2021-001202-M, and the Catalan Agència de Gestió d'Ajuts Universitaris i de Recerca from Generalitat de Catalunya (GENCAT; 2021SGR00671). We acknowledge CSUC ("Consorci de Serveis Universitaris de Catalunya") for allocation of computer resources.

Supporting Information

The Supporting Information is available free of charge at …

Ligand binding mode in the main cavity of monomer A of the COX-2 homodimer, ligand RMSDs, ligand–Arg120 distances, and RMSF of protein residues along MM-MD trajectories, final ligand poses from MM-MD simulations, molecular orbitals of unfolded NANQ-IMC6 in gas phase, energies of S_1 and S_2 along a BOMD simulation of the COX-2 monomer complex, fluorescence spectra from TD-CAM-B3LYP/6-31G(d)/MMPol calculations, comparison of structures along the MM-MD simulations, final structure of the COX-2 homodimer from the MM-MD, fluorescence spectra of NANQ-IMC6 in vacuum, excluding waters, and for the complete hCOX-2:NANQ-IMC6 single monomer and homodimer complexes, including in all cases the contributions of each monomer (A and B) to the dimer spectra, water accessibility analysis, fluorescence spectra of NANQ-IMC6 including the non-realistic initial 100 ns for monomer B, computational protocol designed to simulate the fluorescence spectra of hCOX-2 monomer and homodimer, tables with excited state properties of NANQ computed in vacuum and in different solvents.

References

Anandakrishnan R, Aguilar B, Onufriev AV (2012) H++ 3.0: automating pK prediction and the preparation of biomolecular structures for atomistic molecular modeling and simulations. Nucleic Acids Res. 40:W537-41.

Bayly CI, Cieplak P, Cornell W, Kollman PA (1993) A well-behaved electrostatic potential based method using charge restraints for deriving atomic charges: the RESP model. J. Phys. Chem. 97:10269–10280.

Becke AD (1993) Density-functional thermochemistry. III. The role of exact exchange. J. Chem. Phys. 98:5648–5652.

Braslavsky SE (2007) Glossary of terms used in photochemistry, 3rd edition (IUPAC Recommendations 2006). Pure Appl. Chem. 79:293–465.
Caprasecca S, Curutchet C, Mennucci B PolChat: a polarization-consistent charge fitting tool, ver. 4.1.2. Molecolab Tools; University of Pisa. 2014.
Case DA, Belfon K, Ben-Shalom IY, Brozell SR, Cerutti DS, Cheatham TE (2020) AMBER 2020. 2020.
Cebrián-Prats A, González-Lafont À, Lluch JM (2019) Unraveling the molecular details of the complete mechanism that governs the synthesis of prostaglandin G2 catalyzed by cyclooxygenase-2. ACS Omega 4:2063–2074.
Corbella M, Cupellini L, Lipparini F, Scholes GD, Curutchet C (2019) Spectral variability in phycocyanin cryptophyte antenna complexes is controlled by changes in the α-polypeptide chains. ChemPhotoChem 3:945–956.
Crespo-Otero R, Barbatti M (2018) Recent advances and perspectives on nonadiabatic mixed quantum–classical dynamics. Chem. Rev. 118:7026–7068.
Curutchet C, Muñoz-Losa A, Monti S, Kongsted J, Scholes GD, Mennucci B (2009) Electronic energy transfer in condensed phase studied by a polarizable QM/MM model. J. Chem. Theory Comput. 5:1838–1848.
De Vico L, Anda A, Osipov VA, Madsen AØ, Hansen T (2018) Macrocycle ring deformation as the secondary design principle for light-harvesting complexes. Proc. Natl. Acad. Sci. U. S. A. 115.
Felline A, Seeber M, Fanelli F (2020) webPSN v2.0: a webserver to infer fingerprints of structural communication in biomacromolecules. Nucleic Acids Res. 48:W94–W103.
Fishbein A, Hammock BD, Serhan CN, Panigrahy D (2021) Carcinogenesis: Failure of resolution of inflammation? Pharmacol. Ther. 218:107670.
Frisch MJ, Trucks GW, Schlegel HB, Scuseria GE, Robb MA, Cheeseman JR Gaussian 09. Wallingford CT: Gaussian, Inc; 2009.
Frisch MJ, Trucks GW, Schlegel HB, Scuseria GE, Robb MA, Cheeseman JR Gaussian 16 revision B.01. Wallingford CT: Gaussian, Inc; 2016.
Frisch MJ, Trucks GW, Schlegel HB, Scuseria GE, Robb MA, Cheeseman JR Gaussian development version, revision H.36. Wallingford CT: Gaussian, Inc; 2010.
Gordon JC, Myers JB, Folta T, Shoja V, Heath LS, Onufriev A (2005) H++: a server for estimating pKas and adding missing hydrogens to macromolecules. Nucleic Acids Res. 33:W368-71
Götz AW, Clark MA, Walker RC (2014) An extensible interface for QM/MM molecular dynamics simulations with AMBER. J. Comput. Chem. 35:95–108
Groenhof G, Modi V, Morozov D (2020) Observe while it happens: catching photoactive proteins in the act with non-adiabatic molecular dynamics simulations. Curr. Opin. Struct. Biol. 61:106–112.
Izadi S, Anandakrishnan R, Onufriev AV (2014) Building water models: A different approach. J. Phys. Chem. Lett. 5:3863–3871.
Kim HS, Park T, Ren WX, Lim J-Y, Won M, Heo JS, Lee SG, Kim JS (2018) COX-2 targeting indomethacin conjugated fluorescent probe. Dyes Pigm. 150:261–266.
Kirkby NS, Sampaio W, Etelvino G, Alves DT, Anders KL, Temponi R, Shala F, Nair AS, Ahmetaj-Shala B, Jiao J, et al. (2018) Cyclooxygenase-2 selectively controls renal blood flow through a novel PPARβ/δ-dependent vasodilator pathway. Hypertension 71:297–305.
Kurumbail RG, Stevens AM, Gierse JK, McDonald JJ, Stegeman RA, Pak JY, Gildehaus D, Miyashiro JM, Penning TD, Seibert K, et al. (1996) Structural basis for selective inhibition of cyclooxygenase-2 by anti-inflammatory agents. Nature 384:644–648.

Lahav Y, Noy D, Schapiro I (2021) Spectral tuning of chlorophylls in proteins – electrostatics vs. ring deformation. Phys. Chem. Chem. Phys. 23:6544–6551.
Lee C, Yang W, Parr RG (1988) Development of the Colle-Salvetti correlation-energy formula into a functional of the electron density. Phys. Rev. B Condens. Matter 37:785–789.
Loos P-F, Scemama A, Jacquemin D (2020) The quest for highly accurate excitation energies: A computational perspective. J. Phys. Chem. Lett. 11:2374–2383.
Luo Y, Zhang S, Wang H, Luo Q, Xie Z, Xu B, Tian W (2022) Precise detection and visualization of cyclooxygenase-2 for Golgi imaging by a light-up aggregation-induced emission-based probe. CCS Chem 4:456–463.
Mazzeo P, Hashem S, Lipparini F, Cupellini L, Mennucci B (2023) Fast method for excited-state dynamics in complex systems and its application to the photoactivation of a blue light using flavin photoreceptor. J. Phys. Chem. Lett. 14:1222–1229.
Menter DG, Schilsky RL, DuBois RN (2010) Cyclooxygenase-2 and cancer treatment: Understanding the risk should be worth the reward. Clin. Cancer Res. 16:1384–1390.
Nelson TR, White AJ, Bjorgaard JA, Sifain AE, Zhang Y, Nebgen B, Fernandez-Alberti S, Mozyrsky D, Roitberg AE, Tretiak S (2020) Non-adiabatic excited-state molecular dynamics: Theory and applications for modeling photophysics in extended molecular materials. Chem. Rev. 120:2215–2287.
Nottoli M, Bondanza M, Mazzeo P, Cupellini L, Curutchet C, Loco D, Lagardère L, Piquemal J-P, Mennucci B, Lipparini F (2023) QM/AMOEBA description of properties and dynamics of embedded molecules. Wiley Interdiscip. Rev. Comput. Mol. Sci. 13.
Ozaydin B, Curutchet C (2023) Unraveling the role of thermal fluctuations on the exciton structure of the cryptophyte PC612 and PC645 photosynthetic antenna complexes. Front. Mol. Biosci. 10:1268278.
Rouzer CA, Marnett LJ (2020) Structural and chemical biology of the interaction of cyclooxygenase with substrates and non-steroidal anti-inflammatory drugs. Chem. Rev. 120:7592–7641.
Senge MO, MacGowan SA, O'Brien JM (2015) Conformational control of cofactors in nature – the influence of protein-induced macrocycle distortion on the biological function of tetrapyrroles. Chem. Commun. (Camb.) 51:17031–17063.
Serhan CN, Petasis NA (2011) Resolvins and protectins in inflammation resolution. Chem. Rev. 111:5922–5943.
Serhan CN, Sulciner ML (2023) Resolution medicine in cancer, infection, pain and inflammation: are we on track to address the next Pandemic? Cancer Metastasis Rev. 42:13–17.
Shahrokh K, Orendt A, Yost GS, Cheatham TE 3rd (2012) Quantum mechanically derived AMBER-compatible heme parameters for various states of the cytochrome P450 catalytic cycle. J. Comput. Chem. 33:119–133.
Smith WL, Malkowski MG (2019) Interactions of fatty acids, nonsteroidal anti-inflammatory drugs, and coxibs with the catalytic and allosteric subunits of cyclooxygenases-1 and -2. J. Biol. Chem. 294:1697–1705.
Tian C, Kasavajhala K, Belfon KAA, Raguette L, Huang H, Migues AN, Bickel J, Wang Y, Pincay J, Wu Q, et al. (2020) Ff19SB: Amino-acid-specific protein backbone parameters trained against quantum mechanics energy surfaces in solution. J. Chem. Theory Comput. 16:528–552.
Trott O, Olson AJ (2010) AutoDock Vina: improving the speed and accuracy of docking with a new scoring function, efficient optimization, and multithreading. J. Comput. Chem. 31:455–461.

Qingjing Wang, Xueting Shao, Yuxuan Zhang, Miaojin Zhu, Frederick X. C. Wang, Jianjian Mu, Jiaxuan Li, Hangping Yao, and Keda Chen (2023) Role of tumor microenvironment in cancer progression and therapeutic strategy. Cancer Med.12:11149–11165.

Wang J, Cieplak P, Li J, Hou T, Luo R, Duan Y (2011) Development of polarizable models for molecular mechanical calculations I: parameterization of atomic polarizability. J. Phys. Chem. B 115:3091–3099.

Wang J, Cieplak P, Li J, Wang J, Cai Q, Hsieh M, Lei H, Luo R, Duan Y (2011) Development of polarizable models for molecular mechanical calculations II: induced dipole models significantly improve accuracy of intermolecular interaction energies. J. Phys. Chem. B 115:3100–3111.

Wang J, Wolf RM, Caldwell JW, Kollman PA, Case DA (2004) Development and testing of a general amber force field. J. Comput. Chem. 25:1157–1174.

Wang X, Wang L, Xie L, Xie Z, Li L, Bui D, Yin T, Gao S, Hu M (2020) Design and synthesis of a novel NIR celecoxib-based fluorescent probe for cyclooxygenase-2 targeted bioimaging in tumor cells. Molecules 25:4037.

Wen B, Wei Y-T, Mu L-L, Wen G-R, Zhao K (2020) The molecular mechanisms of celecoxib in tumor development. Medicine (Baltimore) 99:e22544.

Xia W, Zhang S, Li Y, Fan J, Liu B, Wang L, Peng X (2021) Ibuprofen-derived fluorescence inhibitor of COX-2 for breast cancer imaging, prevention and treatment. Dyes Pigm. 190:109326.

Yuan C, Rieke CJ, Rimon G, Wingerd BA, Smith WL (2006) Partnering between monomers of cyclooxygenase-2 homodimers. Proc. Natl. Acad. Sci. U. S. A. 103:6142–6147.

Zhang H, Fan J, Wang J, Dou B, Zhou F, Cao J, Qu J, Cao Z, Zhao W, Peng X (2013) Fluorescence discrimination of cancer from inflammation by molecular response to COX-2 enzymes. J. Am. Chem. Soc. 135:17469–17475.